Digest Journal of Nanomaterials and Biostructures Vol. 19, No. 2, April - June 2024, p. 819 - 835

Temperature effect on improving the carbon fixation properties of steel slag

X. Y. Wang[a], M. Li[a,*], Q. W. Zhan[a,*], X. Zhang[a], Y. M. Ge[b], J. L. Zhou[a]
[a]*School of Civil Engineering and Architecture, Jiangsu University of Science and Technology, Zhenjiang, China*
[b]*School of Civil Engineering, Southeast University, Nanjing, China*

As an important way to reduce CO_2 emissions, mineral carbon dioxide (CO_2) sequestration had received widespread attention. Due to its low cost and secondary use, steel slag (SS) was regarded as a suitable material for carbon fixation. By keeping the pressure, time, and solid-liquid ratio accord, carbon sequestration properties of SS at different temperature were discussed. The composition of the Carbonized Steel Slag (CSS) was analyzed with the aid of XRD and FT-IR. SEM and EDS were utilized to examine the microstructure and elemental distribution of CSS. BET method was employed to analyze the pore characteristics of the CSS. Quantitative analysis of the production was performed in conjunction with TGA. The results revealed that the generated calcium carbonate ($CaCO_3$) was mainly distributed in three places, which were the surface of SS, the external water environment, and the pores inside the slag. At 30 to 60℃, the carbon sequestration capacity was improved with temperature increasing. While the temperature exceeded 60℃, the effect of carbon sequestration was reduced. The results proved that the best effect of carbon sequestration in SS was at 60℃.

(Received February 20, 2024; Accepted June 5, 2024)
Keywords: Steel slag, Temperature, Composition, Microstructure, Carbon fixation

1. Introduction

Steel slag (SS) was one of the major by-products of the iron and steel industry, with its production accounting for 10-15% of crude steel production [1]. According to different production processes, SS could be divided into Basic Oxide Furnace (BOF) slag, Electric Arc Furnace (EAF) slag, and ladle furnace (LF) slag. Among the three types of slags, BOF slag accounted for the vast majority[2]. Analysis based on the World Steel Slag Association (WSSA), worldwide crude steel production reached about 1.84 billion tons, with China accounting for more than half[3]. Incomplete statistics suggested that China produced about 80 million tons of SS annually. However, its reuse rate was only about 30% of the total SS[3][5]. The accumulation of the remaining large amount of SS would cause environmental pollution, waste of resources, and other problems. Due to the presence of free calcium oxide and magnesium oxide in the SS, the volume stability of it was poor. It could not be used directly for construction materials[6][7][8]. In addition, the high content of the RO phase (MnO, FeO, and MgO solid solution) made it difficult to handle[9].

* Corresponding author: zhanqw@just.edu.cn
https://doi.org/10.15251/DJNB.2024.192.819

In order to solve the problems posed by steel slag, numerous scholars have studied it to promote its utilization. Jiao et al. [35] had made direct resource utilization of steel slag. They found that steel slag can be recycled as a smelting material and can also be utilized as a construction material. Due to the presence of calcium and magnesium and other elements in steel slag, it also has a certain carbon sequestration capacity. Bodor et al. [10] discovered that the free MgO and CaO in carbonated steel slag (CSS) were greatly reduced, which improved the stability problem of SS. As a result, some scholars had carried out more detailed researches about the carbon sequestration performance of SS. Chang et al. [11] investigated the relationship between temperature and time. The findings demonstrated that the carbonation period was shortened to 5 minutes to 12 hours at 40℃-160°C. Pan et al. [12] compared the impact of temperature ranges on the carbonation of SS. According to the findings, the carbon fixation capacity would be raised when elevating the temperature, but the rate of calcium carbonate deposition would be decreased. Ji L et al.[13] explored how varied circumstances affected the carbonation of fly ash, including CO2 partial pressure and temperature. The findings indicated that the fastest carbonation reaction rate would be achieved by raising the reaction temperature to 60°C. Tian et al. [36] found that by increasing the temperature from 400°C to 700°C, a dramatic increase in steel slag occurred. Since there were fewer studies on the carbonization of steel slag slurries at different temperatures, this paper focuses on the effect of temperature on the carbonization of steel slag. With the help of micro-analysis, this paper comprehensively analyzes the carbonization mechanism of steel slag slurry and the effect of temperature on the carbon sequestration performance of steel slag.

In this study, carbon sequestration properties of SS at different temperature were discussed by controlling the pressure, time, and solid-liquid ratio consistently. The composition of the CSS was analyzed with the aid of X-ray Diffraction (XRD) and Fourier Transform Infrared-Raman (FT-IR). Scanning Electron Microscope (SEM) and Scanning Electron Microscope (EDS) were utilized to examine the microstructure and elemental distribution of CSS. BET method was employed to analyze the pore characteristics of the CSS. Quantitative analysis of CO_2 was performed in conjunction with Thermalgravimetric Analyzer (TGA). The optimum reaction temperature of SS was determined by the measurement of XRD, FT-IR, SEM-EDS, BET, and TGA.

2. Materials and methods

2.1. Raw materials

In this experiment, the converter SS produced by Henan Anyang Iron and Steel Group Liability Co., Ltd was in application. The SS exhibited a specific surface area of 1.116m²/g, as determined using a laser particle sizer for analysis. The results of the test were was illustrated in Fig.1. From Fig.1, the particle size of SS mainly fell within the spectrum of 1 to 40 μm. Since D10 was 2.57 μm, D50 was 10.97 μm, and D90 was 35.50 μm, it had a greater specific surface area. Consequently, it would be more reactive.

In this experiment, the substance composition of the SS was investigated with the aid of X-ray Fluorescence spectroscopy (XRF). The composition was illustrated in Table 1. The SS primarily consisted of CaO, Fe_2O_3, SiO_2, and Al_2O_3 from Fig. 1. The CaO content in the SS was found to be 30.82%, which could act as a sufficient calcium source for the carbon sequestration reaction.

Table 1. Main chemical composition of SS (%).

Material	Na_2O	MgO	Al_2O_3	SiO_2	P_2O_5	SO_3	CaO	Fe_2O_3	K_2O
Content	0.39	5.81	8.55	21.55	0.54	0.61	30.82	24.74	0.17

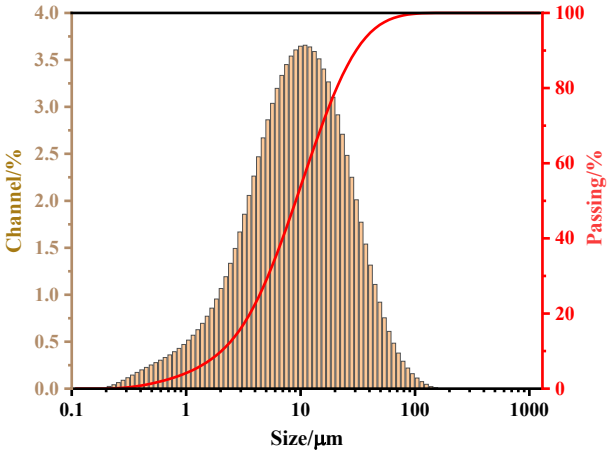

Fig. 1. Particle size distribution of SS.

2.2. CO_2 fixation process

Carbon fixation was performed utilizing the apparatus depicted in Fig. 2. It primarily consisted of the reaction vessel, the gas blending tank, the gas injection system, and a data acquisition system. The reaction vessel was covered with the heating device to heat the samples. Two tubes were installed on both sides of the reactor for gas injection. A probe was introduced from the reactor's upper section to monitor the pressure and temperature within the chamber. Real-time display of the internal conditions of the reactor was achieved through a data detection system.

After thorough mixing 1 gram of SS with 10 grams of water, the mixture was transported into a carbon fixation device. The heating device was started to heat up to the required temperature for the experiment. Then, CO_2 at a purity level of 99% was gassed into the reactor when the pressure was below 0.2MPa. After reacting fully for one hour, took out and put it into the oven to dry for 24h.

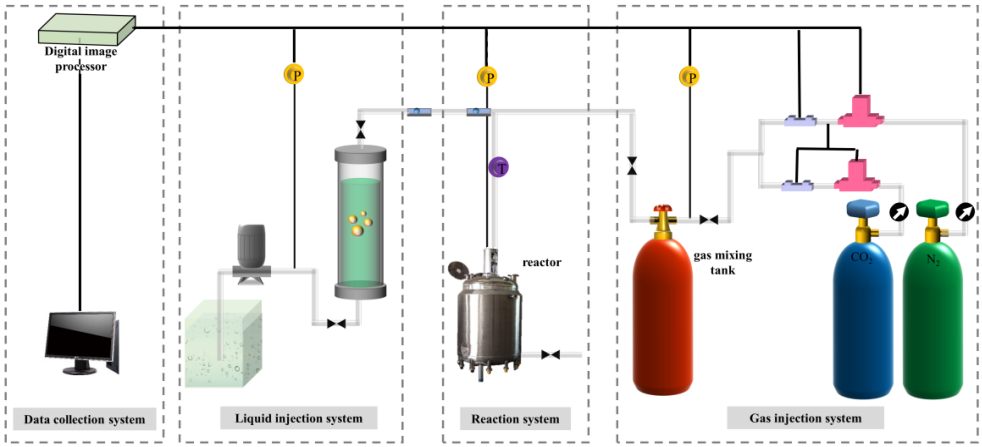

(a)

(b)

Fig. 2. (a) flowchart of the CO_2 fixation (b) Physical drawing of the device.

2.3. Microscopic characterization methods

The mineral composition of the carbonation CSS was characterized with the aid of XRD and FTIR. Within a specific timeframe, CSS was grinded with acetone to stop the reaction in accordance with the way of RILEM TC-238 [17][18]. After the CSS was powdered until they could pass through a 200 Mesh sieve, they were measured. In this experiment, the crystal composition of CSS was analyzed using the X-ray diffractometer model TD-3500. The angle tested ranged from 5° to 85° with an increment of 0.2 seconds. FTIR-650S was employed to measure the functional group composition in CSS, with a wavelength range tested from 4000-400 cm^{-1}.

The microstructure of the CSS was observed by COXEM EM-30 Scanning Electron Microscope. For SEM measurements, the sample was uniformly covered with gold powder to boost conductivity for better observation. Subsequently, the sample was tested under an accelerating voltage of 15 kV. The distribution of elements on the sample was tested using EDS.

The pore structure of CSS was tested using equipment with the model V-sorb 2800, which was in line with the BET method. Subsequently, the sample was initially degassed at 70°C for 1 hour to minimize the influence of pore water. Following that, the treated sample was placed in a liquid nitrogen environment for nitrogen adsorption experiments using the BET method. Finally, adsorption-desorption experiments were conducted at various pressures to obtain the pore characteristics of the sample.

2.4. Quantitative analysis of CO_2

The carbon fixation capacity of SS was evaluated using the TGA. Firstly, approximately 10mg of the sample was weighed and placed on a microbalance. Subsequently, the sample was heated from room temperature to 100°C, and the specific weight loss range and mass of the sample were recorded. The weight loss of samples at 520-850°C was recorded by microbalance, which was used to calculate the carbon sequestration using Equation (1)[8][28].W_1 was the temperature of $CaCO_3$ in DTG when it started to absorb heat. W_2 was the temperature at which $CaCO_3$ in DTG ended up absorbing heat.

$$CO_{2uptake} = \frac{W_1 - W_2}{W_2} \times 100 \quad (1)$$

According to Steinour's [14] formula, the theoretical maximum carbon fixation of the SS was determined to be 244.4 Kg/t by the content of CaO, Na_2O, K_2O, and SO_3.

Steinour formulas：

$$Q_t = 0.785(CaO - 0.7SO_3) + 1.09Na_2O + 0.93K_2O \quad (2)$$

3. Results and discussion

3.1. Composition of the product

The XRD patterns of CSS at different reaction temperature and uncarbonized SS were depicted in Fig.3 As was apparent from it, the SS was predominantly consisted of $Ca_2Fe_2O_5$ (C_2F), $CaCO_3$, Ca_2SiO_4 (C_2S), FeO, 2CaO-Al_2O_3-SiO_2 (C_2AS), Ca_3SiO_5 (C_3S), and the RO phase. According to the Fig. 3, the intensity of the diffraction peaks of $CaCO_3$ around 30° was enhanced and the number of them increased dramatically. A substantial amount of $CaCO_3$ resulted from the reaction between CO_2 and silicate minerals, including the amorphous phases rich in calcium. [19][20]. These $CaCO_3$ had different crystal forms, respectively Calcite, Vaterite and Aragonite. The diffraction peaks for Calcite manifested around 29°, 36°, 39°, 42°, 47°, and 48°.At the same time, the diffraction peaks of Vaterite occurred near 26°,44° and 50°. The diffraction peaks of Aragonite occurred near 33°. As could be seen in Fig.3, $CaCO_3$ was the only detected crystalline phase product after carbonization. Normally calcium-and magnesium-containing alkaline minerals had carbonation reactivity, but the crystalline phase carbonate with magnesium was not detected by XRD. In fact, it was shown that precipitation of $MgCO_3$ needs to be generated at temperatures greater than 144°C and P_{CO2} greater than 10 MPa[30][31]. On the contrary, the diffraction peaks of C_2S were weaker and fewer in number. The diffraction peaks of CaO weakened after carbonization, and the intensity of the diffraction peaks decreased with raising temperature. The primary material

involved in the carbonation reaction was C_2S and C_3S, which was evidenced by the fact that the diffraction peaks of C_2S and C_3S diminished around the angle of 32°. The diffraction peak positions of XRD at different reaction temperatures were basically the same, but the diffraction peak intensities were slightly changed. In the range of 30-60°C, the peak intensity of $CaCO_3$ near 30° were increased with temperature increasing. However, the peak intensity near 30° was decreased with temperature increasing in the range of 60-70℃.

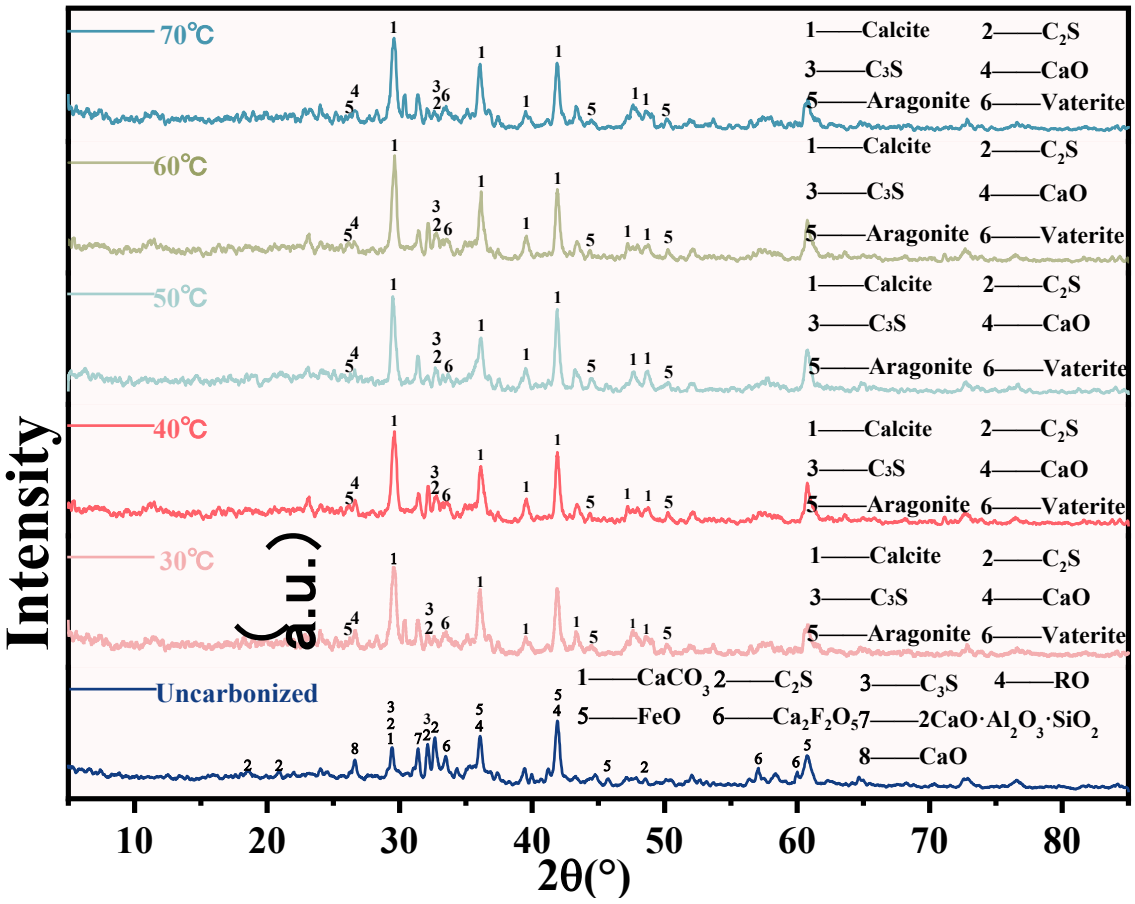

Fig. 3. XRD patterns of CSS at different reaction temperature and uncarbonized SS.

FT-IR measurements were conducted in the paper to obtain a better understanding of the product, with absorption in the 500-4000 cm^{-1} wavelength region. The statistical results of the test were illustrated in Fig. 4. With the exception of intensity, the positions of the diffraction peaks of CSS at various reaction temperature were essentially the same. The results showed that the mineral composition of CSS was essentially the same, which was in line with the analysis of XRD.

The broad and intense bands observed above 3000 cm^{-1} and approximately at 1650 cm^{-1} were assigned to the bending and stretching vibrations associated with O-H functional groups. [21][22]. A board peak was observed in Fig.4 near 3435 cm^{-1}, which was the symmetric and antisymmetric stretching vibration absorption bands of O-H. According to the diffusion characteristics, it was a poorly crystallized phase or bound water[23]. A great deal of $CaCO_3$ was produced in the product, which was corresponded to 3 kinds of vibrate. The first one was the

out-of-plane bending vibration of the C-O, which appeared at 870 cm^{-1}. The second one was the in-plane bending vibration of the C-O at the corresponding wave of 712 cm^{-1}. The final one was the asymmetric stretching vibration band of the C-O at 1426 cm^{-1}[15][16]. According to morphology, $CaCO_3$ could be divided into calcite, aragonite, and vaterite, which were correlated to the three C-O vibrations in FTIR. Among the 3 types of $CaCO_3$, calcite was the most stable one. It could be seen from Fig.4 that the peaks at 1428, 872, and 712cm^{-1} were shifted and steeper as the temperature increased. This suggested that an increase in reaction temperature had a promoting effect on the crystallinity of $CaCO_3$[32].

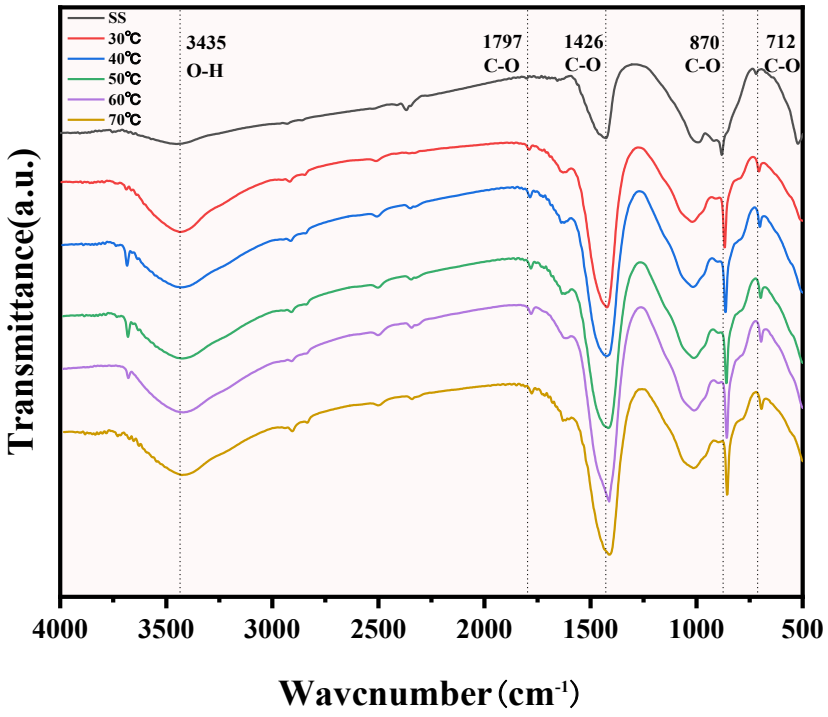

Fig. 4. Infrared spectrum of CSS at different reaction temperature and uncarbonized SS.

3.2. Microstructure and elemental distribution of CSS

The microscopic organization and elemental distribution of the CSS were investigated with the aid of SEM-EDS. The results of the tests were depicted in Fig. 5.

According to the results of Fig. 9(a), the surface of SS was discovered to be generally smooth with a few small particles adhering to the surface. However, the surface would be covered with more small particles as the reaction process further. The SEM images before and after carbonization showed that the steel slag particles were bonded together after carbonization. As shown in the results of the element distribution, the primary constituents of the minuscule particles included O, C, Ca, Mg, and Fe. The major crystalline phases formed could be seen as $CaCO_3$ by the atomic ratios. The presence of carbonation products attached to the particle surface could influence the precipitation of Ca^{2+} and Mg^{2+}. It would eventually affect the carbonation.[24]. When the reaction temperature was increased, more and more small particles covering the surface of SS could be observed from Fig. 5(b) to (f). There were still uncovered areas covering the SS exterior

during the temperature was 30 to 50°C. However, at temperatures of 60 to 70°C, the surface of the SS was nearly entirely wrapped. Alternatively, the nucleation of calcium carbonate crystals was accelerated after the temperature rose. The sample morphology tended to be irregular[34] when the growth rate was faster. It could be seen from Fig.5(e) to (f). As analyzed in XRD, in Fig.5 different morphologies of $CaCO_3$ could be observed including calcite, aragonite, and vaterite. Some of the $CaCO_3$ produced by carbonization covered the SS surface, while others formed calcite, spherulite, and aragonite individually. From a different perspective, the nucleation of calcium carbonate crystals was accelerated after the temperature rise. When the growth rate was faster, the sample morphology tended to be irregular.

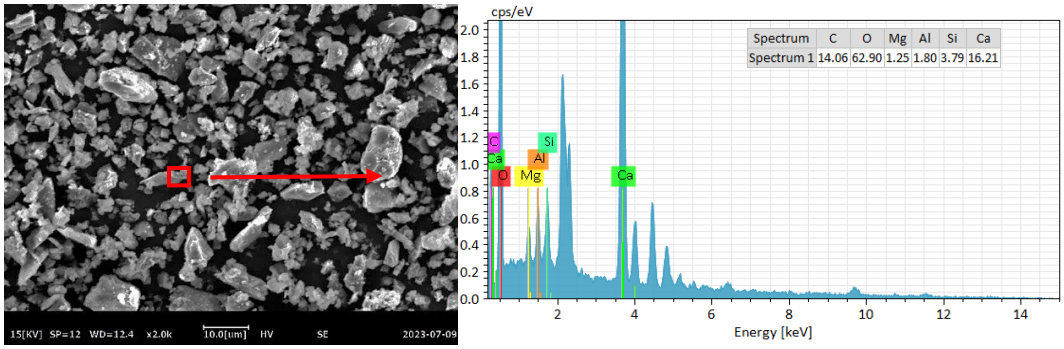

(a) SS

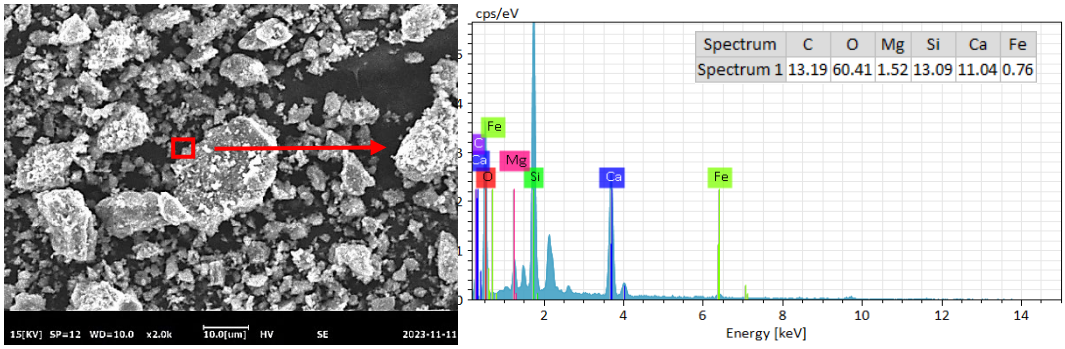

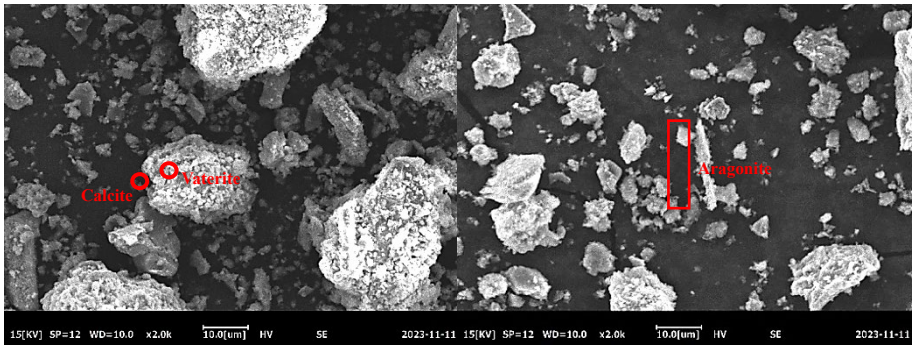

(b) CSS at 30°C

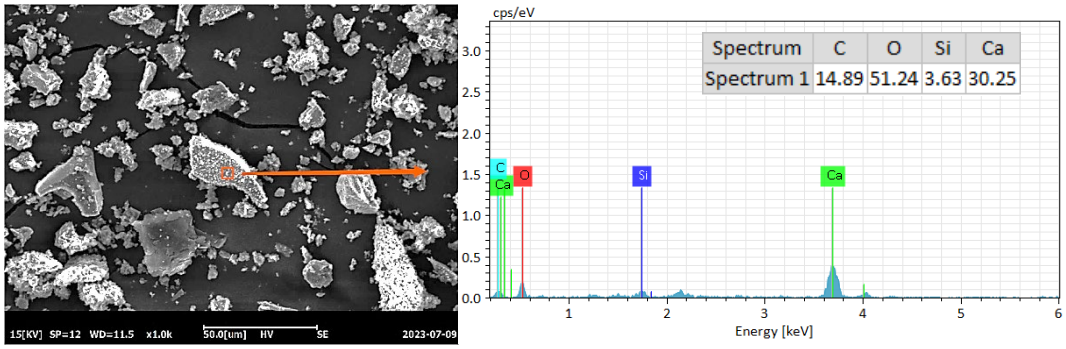

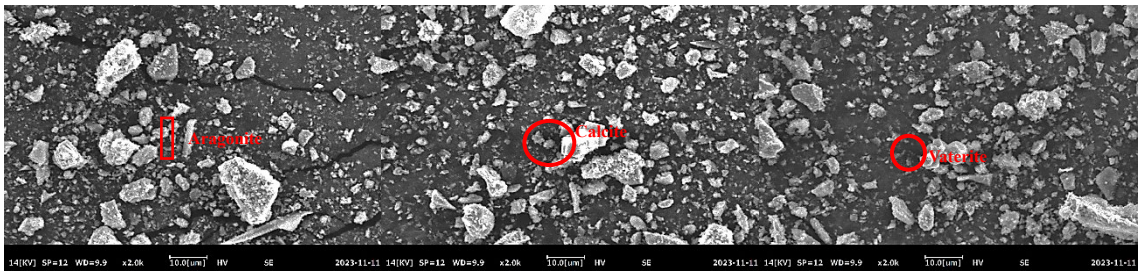

(c) CSS at 40°C

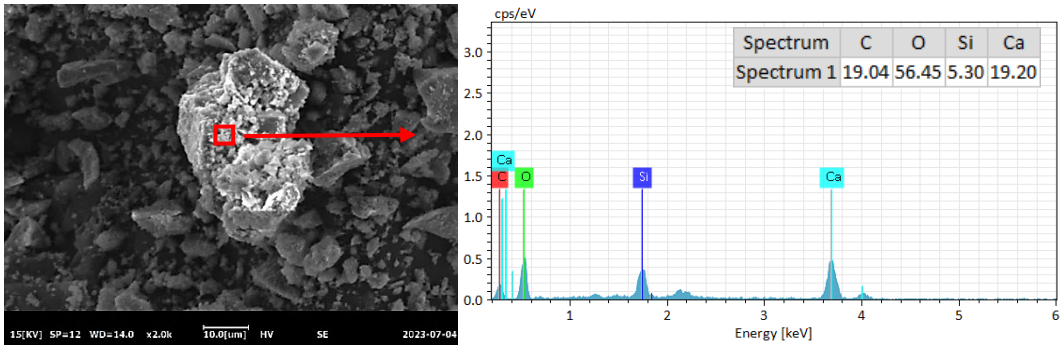

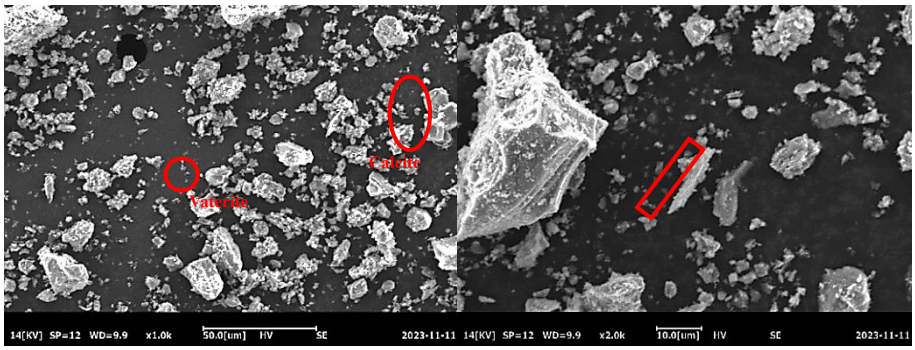

(d) CSS at 50°C

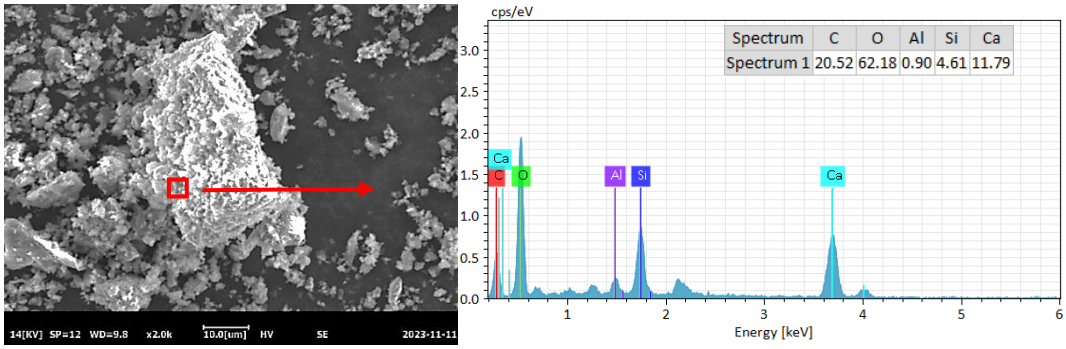

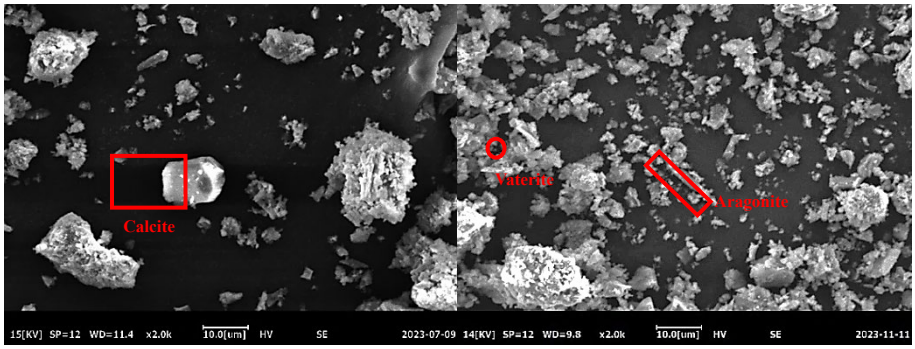

(e) CSS at 60°C

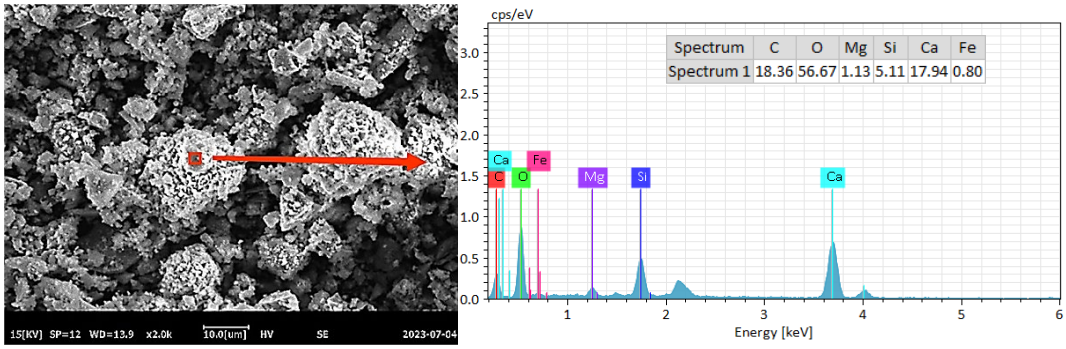

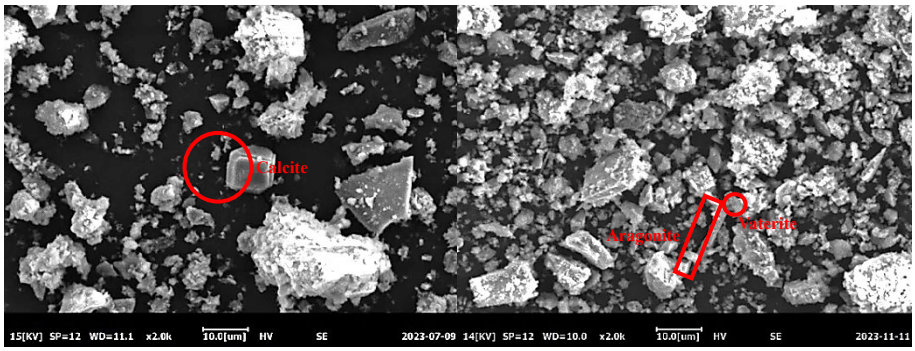

(f) CSS at 70°C

Fig. 5. Microstructure and elemental distribution of SS and CSS.

3.3. Pore characteristics of CSS

The results of the V-Sorb 2800 test were depicted in Fig.6 and Fig.7, which were carried out to observe the pore size variations of the CSS and SS. In accordance with the Kelvin equation, the micropores sequentially were filled at extremely low pressure ($P/P_0 < 10^{-2}$). When the pressure was low, nitrogen adsorbed on the surface of micropores in a monolayer configuration. As the pressure rose, multilayer adsorption appeared, and capillary coalescence started to take place. The capillary coalescence occurred when very high pressure was reached. Following the completion of adsorption, the desorption of the sample commenced. According to Fig.6, all of the adsorption-desorption isotherms grew gradually when the pressure fell below 0.9. In accordance with the classification of the IUPAC, adsorption isotherms of each sample were typical type III isotherms [25][26]. As a result of the differing pressure levels, adsorption return lines were produced with coalescence and evaporation adsorption isotherms branching. The properties of the pore size of the material were reflected by the shape of the return lines. As shown in Fig.6, a clear "hysteresis loop" was displayed in the adsorption-desorption isotherms of the samples. According

to the categorization system of the IUPAC, all of the samples displayed hysteresis loops of the H2-type, which were relatively narrow. The desorption isotherms essentially were followed by the adsorption isotherms without any evident turning points. The phenomenon indicated that the pore sizes of the material were more restricted. It was matched to the pore of the well-connected space, such as the cylindrical and elliptical nanoscale pores. As can be observed in the following figure, the adsorption and desorption curves of the CSS were higher than before. It could be evident from Fig. 7 that the aperture of SS was too large on the whole. Due to the infiltration of carbonated products into certain pores of the SS, the sample experienced a reduction in pore size. The adsorption capacity was boosted with the specific surface area increased and pore volume decreased[37].

When it comes to low-temperature liquid nitrogen adsorption-based pore structure investigation, the BB Hodote pore classification method was widely utilized. According to the size of the hole, it could be divided into five types. The first type was micropores, which size was less than 10nm. The second type was small pores, with their size at 10-10^2nm. The third type was medium pores, which size was at 10^2-10^3nm. The fourth type was macropores, with its size at 10^3-10^5nm. The last type was visible pores, which size was over 10^5nm[27]. The pore distributions were primarily divided into the bimodal distribution and several tiny peak patterns. When the temperature was at 40-60℃, the multi-peak mode was appeared, with a nanoscale pore size distribution of 180nm. It generally had two or three tiny peaks, which were between 2 and 5nm. The pore size distribution was minimal, and the remaining intervals lacked peaks. The temperature distribution at 30°C and 70°C was bimodal, with several tiny peaks and a single major peak. Within 228 nm, the nanoscale pore size distribution was primarily composed of several minor and large peaks. The peaks were evenly spaced between 2 and 7nm, with no peaks occurring at other intervals. The pore size distribution had a modest magnitude. As could be seen from the pore size distribution, the CSS had fewer large pores and more small pores. It suggested that some of the pores were filled with $CaCO_3$, which improved the mechanical properties of the SS.

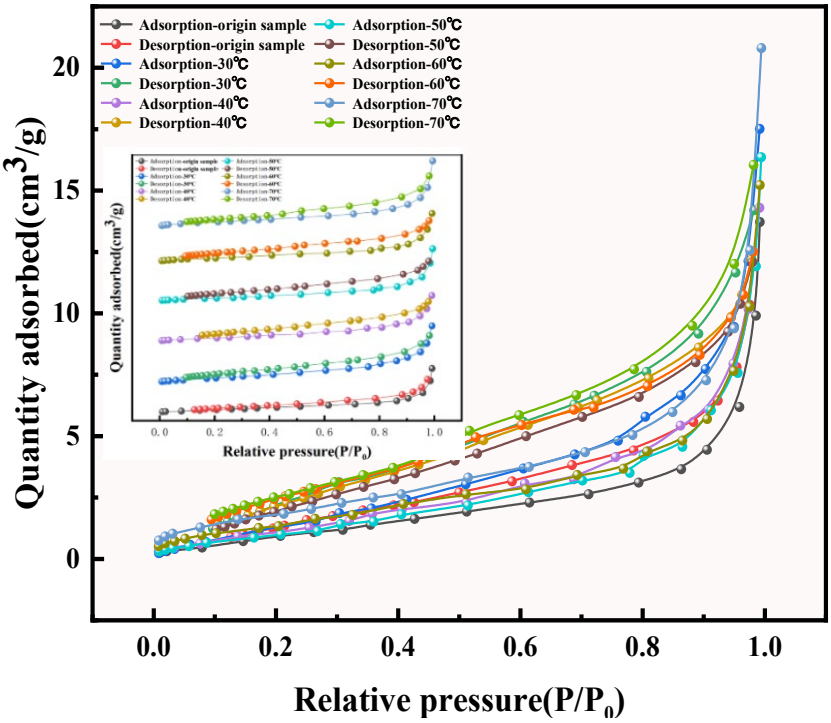

Fig. 6. Adsorption-desorption isotherm chart.

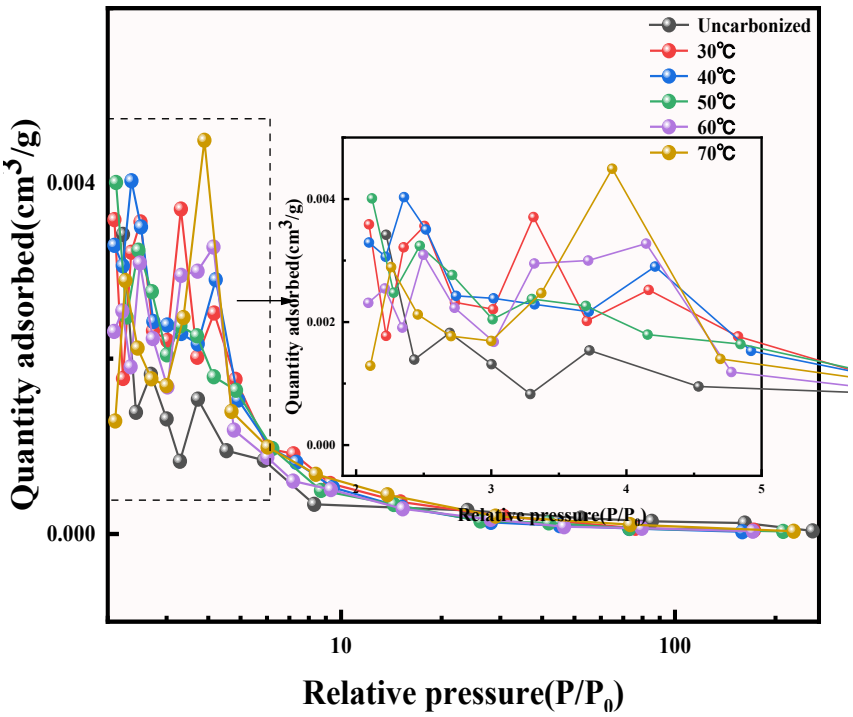

Fig. 7. Pore size distribution of CSS and SS.

3.4. Carbon sequestration

Further TGA testing was conducted on SS to explore the extent of CO_2 fixation, as depicted in Fig. 8 and 9. According to the DTG curves, the heat absorption peak at 310-450°C was associated with the decomposition of Ca $(OH)_2$. According to Equations 3 and 4, Ca $(OH)_2$ was produced by the hydration of C_2S and C_3S. Chang at el. [29] found that the content of Ca $(OH)_2$ was increased with the hydration of C_2S and C_3S.

$$2CaO \cdot SiO_2 + mH_2O \rightarrow xCaO \cdot SiO_2 \cdot yH_2O + (2-x)Ca(OH)_2 \quad (3)$$

$$3CaO \cdot SiO_2 + mH_2O \rightarrow xCaO \cdot SiO_2 \cdot yH_2O + (3-x)Ca(OH)_2 \quad (4)$$

However, the diffraction peaks of calcium hydroxide were not found in XRD, which may be related to sampling. The heat absorption peaks at 310-450°C were absent when the reaction temperature was 40-70°C. It indicated that Ca $(OH)_2$ was not produced in the carbonation product, which was matched with the results of the XRD analysis. A distinct heat absorption peak was observed between 520 and 850°C at a reaction temperature of 30-70℃. The heat absorption peak that occurred between 520 and 850°C was more pronounced at 60°C.

As could be seen in Fig.9, a tiny step between 310 and 450°C was formed at the reaction temperature of 30°C. The step was corresponded to the weight loss of the decomposition of Ca $(OH)_2$, which was matched with the DTG curve. Meanwhile, a significant weight loss step between 520 and 850℃ was observed at 30-70℃, corresponding to the weight loss of the decomposition of $CaCO_3$. The weight loss of $CaCO_3$ between 520 and 850℃ was used to compute the CO_2 uptake. CO_2 sequestration was counted by Equation (1). At 520-850℃, the mass loss rate of CSS at 60℃ was 9.651%, which was higher than CSS at other temperature. It could be calculated that each gram of SS could be fixed with 0.110g CO_2 by using Equation (1). The CSS lost the least weight at 30℃, reaching 7.413% . According to Equation (1), it could be calculated that each gram of SS can be fixed with 0.081g CO_2. The most rapid change in weightlessness

occurred at 40-50℃, with carbon fixation per gram of SS increased from 0.089g to 0.105g. At 30-60℃, the carbon sequestration per gram of SS was generally increased. However, when the temperature rose from 60℃to 70℃, the amount of carbon sequestration decreased, reaching 0.103g. The statistics of carbon fixation in steel slag at different reaction temperatures was showed in Fig.10.

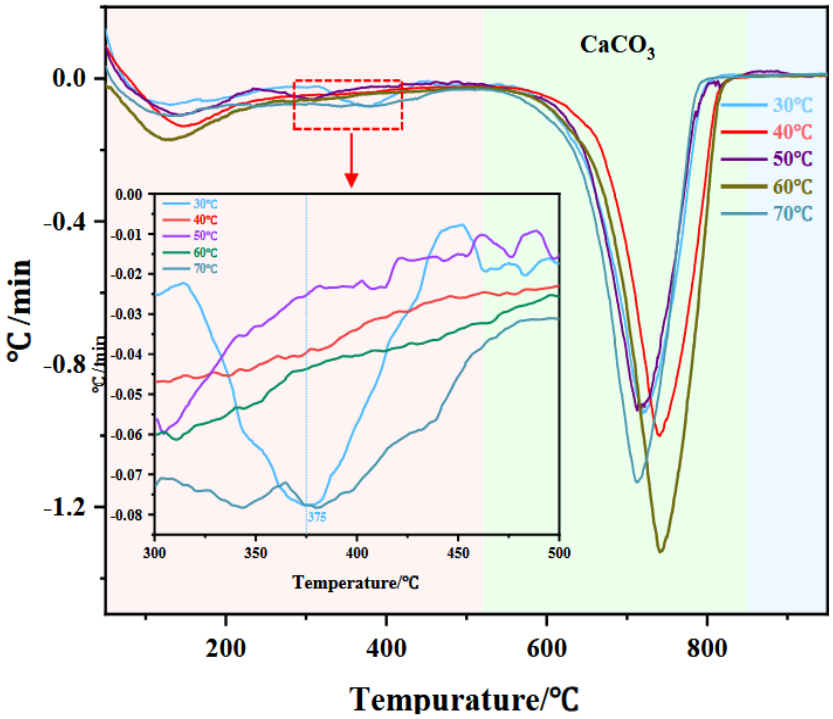

Fig. 8 DTG curves of the CSS.

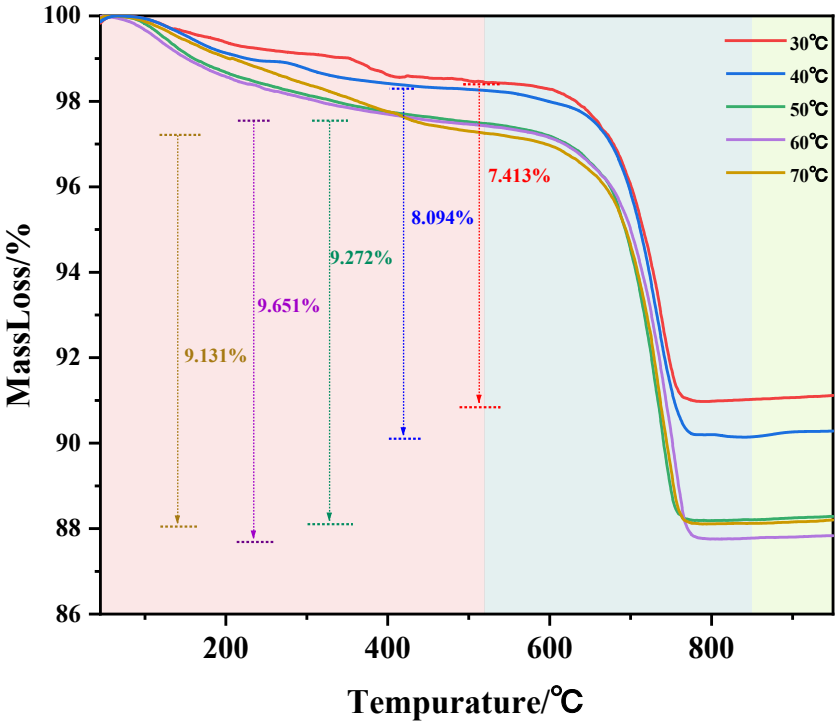

Fig. 9. TG curves of the CSS.

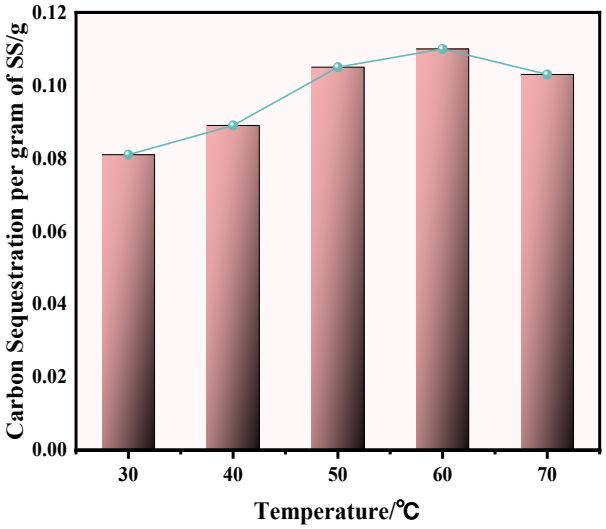

Fig. 10. Graph of carbon sequestration statistics.

3.5. Carbon sequestration mechanism and temperature action mechanism of SS

Due to the low cost and secondary use of SS, it was regarded as a suitable material for carbon fixation. The carbon sequestration capability of SS at various temperatures was investigated in this article, with its carbon fixation mechanism exhibited in Fig. 11. The fixation of CO_2 was divided into three stages. At first, the SS and water came into contact, and Ca^{2+} was released with the hydration of C_2S and C_3S. Then, H_2CO_3 was produced by the interaction of CO_2 and water, and the CO_3^{2-} was eventually formed with the loss of H^+. Finally, $CaCO_3$ was produced when Ca^{2+} and CO_3^{2-} made contact. Temperature could have a serious effect on all three stages. Raising the temperature would increase the rate of CO_2 diffusion and dissolution, and the dissolution rate of Ca^{2+} increased at the same time[33]. The rate of reaction between CO_3^{2-} and Ca^{2+} also increased with raising temperature, and it also facilitated carbonate nucleation and growth of calcium[34]. All these perspectives can explain the increase in temperature in favor of carbonization efficiency. On the other hand, an increase in temperature also decreased the solubility of CO_2. As found in TG, the carbonization effect of steel slag decreased when the temperature increased from 60°C to 70°C. In the first step of the reaction, the Ca^{2+} released from the SS was distributed in three main places. A portion of free Ca^{2+} was concentrated and gathered in the surface layer of SS. Some of them were in the internal pore water. The other was in the external aqueous environment. Consequently, there were three ways to produce $CaCO_3$. Some of the $CaCO_3$ was attached to the surface of the SS. Some of them were dispersed throughout the surrounding aqueous environment, and the others were generated in the pores of SS. When the temperature rose, the amount of carbon fixation in the SS also rose. However, the impact of carbon fixation would be lessened when raising the temperature to a particular level. In this paper, a study was made on the temperature, and the carbon sequestration capacity could also be increased by increasing the time and pressure.

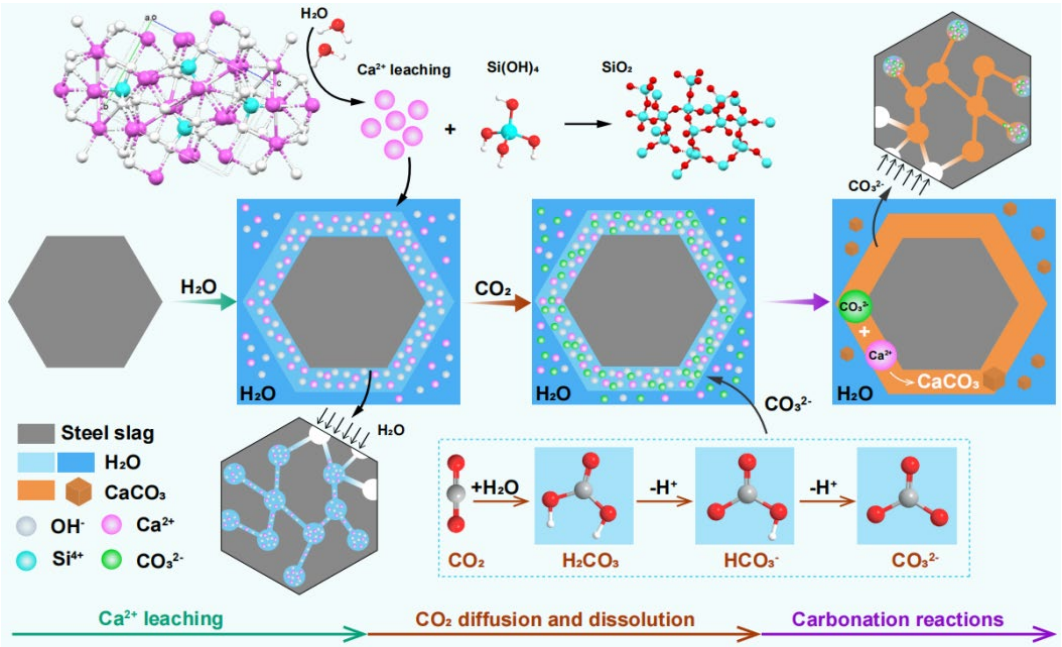

Fig. 11. The carbon fixation mechanism diagram for CO_2.

4. Conclusion

The carbon sequestration capability of SS at various temperatures was investigated in this article. Based on the discussion above, the following conclusions could be drawn.

First of all, Ca $(OH)_2$ produced by the hydration of steel slag at 30°C could not be completely reacted. A small quantity of Ca $(OH)_2$ was evidenced in DTG curves in the final product. However, no Ca $(OH)_2$ was found at temperature between 40 and 70℃. Secondly, the effect of carbon sequestration was the best when the reaction temperature was 60°C, reaching 0.110g/g. However, the effect of carbon sequestration was reduced at 70℃. Carbon fixation rose fastest in the 40-50°C range. Thirdly, it could be seen that $CaCO_3$ generated after carbonization had three crystal structures, which were calcite, aragonite and vaterite. The presence of carbonation products attached to the particle surface could influence the precipitation of Ca^{2+} and Mg^{2+}, which would have an adverse impact on the progress of the carbonization reaction. At last, the internal pores of SS would undergo further reduction due to the filling of carbonization products. Because of this, the aperture inside the SS became smaller, which would improve the mechanical properties of the SS.

Acknowledgements

This work was supported financially by Natural Resources Development Special Foundation of Jiangsu Province (Grant No. JSZRHYKJ202113), National Nature Science Foundation of China (Grant No. 51908253), Jiangsu Graduate Research and Practice Innovation Program (Grant No. KYCX24_4137).

References

[1] R. Ragipani, S. Bhattacharya, A.K. Suresh, React. Chem. Eng, 6 (7), 1152-1178 (2021); https://doi.org/10.1039/D1RE00035G

[2] Y Jiang, T.C Ling, C.J Shi, S.Y Pan, Resources Conservation &Recycling, 136, 187-197 (2018); https://doi.org/10.1016/j.resconrec.2018.04.023

[3] X. Liang, Lin Q, Jiang M, Appl. Energy, (2020).

[4] O. Gencel, O. Karadag, OH. Oren, T. Bilir, Constr. Build. Mater, 283, 122783 (2021); https://doi.org/10.1016/j.conbuildmat.2021.122783

[5] L. Kang, H.L. Du, H. Zhang, W.L. Ma, Complexity, 2018,6703908 (2018); https://doi.org/10.1155/2018/6703908

[6] J. Hu,. Anal. Calorim. 128 (3), 1251-1263 (2017); https://doi.org/10.1007/s10973-017-6107-9

[7] H.J. Zhu, M.Y. Ma, X.Y. He, Z.Q. Zheng, Y. Su, J. Yang, H. Zhao, Constr. Build. Mater, 286, 122823 (2021); https://doi.org/10.1016/j.conbuildmat.2021.122823

[8] L.W. Mo, F. Zhang, M. Deng, F. Jin, A. Al-Tabbaa, A. Wang, Cem. Concr. Compos. 83,138-145 (2017); https://doi.org/10.1016/j.cemconcomp.2017.07.018

[9] C. Shi, Cheminform. 16 (3), 230-236 (2004); https://doi.org/10.1061/(ASCE)0899-1561(2004)16:3(230)

[10] M. Bodor, R.M. Santos, L. Kriskova, J. Elsen, M. Vlad, T.V, Gerven, Mineral, 25 (4), 533-549 (2013); https://doi.org/10.1127/0935-1221/2013/0025-2300

[11] E.E. Chang, S.Y. Pan, Y.H. Chen, H.W. Chu, C.F. Wang, P.C. Chiang, Hazard. Mater, 195, 107-114 (2011); https://doi.org/10.1016/j.jhazmat.2011.08.006

[12] K.W. Chen, S.Y. Pan, C.T. Chen, Y.H. Chen, P.C. Chiang, Clean. Pro, 124, 350-360 (2016); https://doi.org/10.1016/j.jclepro.2016.02.072

[13] L. Ji, H. Yu, B. Yu, R.J Zhang, D. French, M. Grigore, X.L. Wang, Z.L. Chen, S.F. Zhao, Ener. Fuel, 32 (4), 4569-4578(2018); https://doi.org/10.1021/acs.energyfuels.7b03137

[14] J.G. Jang, G.M. Kim, H.J. Kim, H.K. Lee, Constr. Build. Mater, 127, 762-773 (2016); https://doi.org/10.1016/j.conbuildmat.2016.10.017

[15] W. Ashraf, J. Olek, Mater. Sci, 51 (13), 6173-6191(2016); https://doi.org/10.1007/s10853-016-9909-4

[16] P. Jin, R. Wang, Y. Su, H. Dong, Q. Wang, Constr. Build. Mater, 228, 117110 (2019); https://doi.org/10.1016/j.conbuildmat.2019.117110

[17] Z. Sun, A. Vollpracht. Cem. Conc. Res, 103, 110-122 (2018); https://doi.org/10.1016/j.cemconres.2017.10.004

[18] K.L. Scrivener, B. Lothenbach, N. De Belie, E. Gruyaert, J. Skibsted, R. Snellings, A. Vollpracht. Mater. Struct, 48(4), 835-862 (2015); https://doi.org/10.1617/s11527-015-0527-4

[19] C. Shi, F. He, Y. Wu, Constr. Build. Mater, 26(1), 257-267 (2012); https://doi.org/10.1016/j.conbuildmat.2011.06.020

[20] D. Wang, Y.F. Fang, Y.Y. Zhang, J. Chang, J. CO2 Util, 34, 149-162 (2019); https://doi.org/10.1016/j.jcou.2019.06.005

[21] B. Walkley, R. San Nicolas, M.A. Sani, G.J. Rees, J.V. Hanna, J.S.J. van Deventer, J.L. Provis, Cem. Conc. Res, 89, 120-135 (2016); https://doi.org/10.1016/j.cemconres.2016.08.010

[22] M. Criado, A. Fernandez-Jimenez, A. Palomo, Micropor. Mesopor. Mater, 106 (1), 180-191

(2007); https://doi.org/10.1016/j.micromeso.2007.02.055

[23] E. Kapeluszna, L. Kotwica, A. Rozycka, L. Golek, Constr. Build. Mater, 155, 643-653 (2017); https://doi.org/10.1016/j.conbuildmat.2017.08.091

[24] T. Sevelsted, J. Skibsted, Cement and Concrete Research, 71, 56-65 (2015); https://doi.org/10.1016/j.cemconres.2015.01.019

[25] K.W. Sing, Pure. Appl. Chem, 57 (4), 603-619 (1985); https://doi.org/10.1351/pac198557040603

[26] Y.S. He, Z. Li, H.X. Xi, J.G. Guo, Q.B. Xia, Ion Exchange and Adsorption. 20(4), 376-384(2004).

[27] Q. Hao, China Coal Society, 12 (4), 51-57 (1987).

[28] G. Liu, K. Schollbach, P.P. Li, H.J.H. Brouwers, Constr. Build. Mater, 280, 122508 (2021); https://doi.org/10.1016/j.conbuildmat.2021.122508

[29] B.X. Zhang, P. Zhang, J. Chang, Concrete, 2022 (10), 75-78 (2022).

[30] E. Chang, C Anchia, S Pan, International Journal of Greenhouse Gas Control, 12, 382-389 (2013); https://doi.org/10.1016/j.ijggc.2012.11.026

[31] T. Sevelsted, J Skibsted, Cement and Concrete Research, 71, 56-65(2015); https://doi.org/10.1016/j.cemconres.2015.01.019

[32] X. Zhang, C.X. Qian, Z.Y. Ma, F. Li, Construction and Building Materials, 326, 126864 (2022); https://doi.org/10.1016/j.conbuildmat.2022.126864

[33] B. Wu, Y.H. Liang, Journal of Natural Disasters, 19(1), 36-42 (2010).

[34] Lee, T.J, Hong, Cryst Growth Design, 15(4), 1652-1657 (2015); https://doi.org/10.1021/cg501419e

[35] W. Jiao, A. Sha, Z. Liu, W. Li, W. Jiang, W. Qin, Y. Hu, Clean. Prod, 277, 123574 (2020); https://doi.org/10.1016/j.jclepro.2020.123574

[36] S. Tian, J. Jiang, X. Chen, F. Yan, K. Li, Chem Sus Chem 6 (12), 2348-2355 (2013); https://doi.org/10.1002/cssc.201300436

[37] J.R. Shen, Q.J. Xu, Material Reports, Vol.34, No. 1 (2020).